

# Rotational Phonons Drive Low-Energy Kinks in Cuprate Superconductors

Yanyong Wang,<sup>1,\*</sup> Manuel Engel,<sup>2,\*</sup> Christopher Lane,<sup>3</sup> Henrique Miranda,<sup>2</sup>  
Lin Hou,<sup>1</sup> Bernardo Barbiellini,<sup>4,5,6</sup> Adrienn Ruzsinszky,<sup>1</sup> John P. Perdew,<sup>1</sup>  
Robert S. Markiewicz,<sup>5,6</sup> Arun Bansil,<sup>5,6,†</sup> Jianwei Sun,<sup>1,‡</sup> and Ruiqi Zhang<sup>1,§</sup>

<sup>1</sup>*Department of Physics and Engineering Physics,  
Tulane University, New Orleans, LA 70118, USA*

<sup>2</sup>*VASP Software GmbH, Berggasse 21/14, 1090 Vienna, Austria*

<sup>3</sup>*Theoretical Division, Los Alamos National Laboratory, Los Alamos, New Mexico 87545, USA*

<sup>4</sup>*Department of Physics, School of Engineering Science,  
LUT University, FI-53850 Lappeenranta, Finland*

<sup>5</sup>*Department of Physics, Northeastern University, Boston, MA 02115, USA*

<sup>6</sup>*Quantum Materials and Sensing Institute, Northeastern University, Burlington, MA 01803, USA*

Angle-resolved photoemission spectroscopy (ARPES) reveals ubiquitous quasiparticle “kinks” near  $\sim 70$  meV and  $\sim 40$  meV across cuprate superconductors, often accompanied by peak–dip–hump (PDH) structures. These features point to strong coupling between electrons and low-energy bosonic excitations, but the microscopic origin has remained elusive due to the limitations of conventional density-functional theory (DFT) and the high cost of beyond-DFT methods. Here, we systematically study the electron–phonon coupling (EPC) in hole-doped infinite-layer  $\text{CaCuO}_2$  using the Strongly Constrained and Appropriately Normed (SCAN) density functional, explicitly including magnetic effects. We find a substantial EPC strength  $\lambda$  of  $\sim 0.5$  in the magnetic phase, producing kinks and PDH structures in the 40–80 meV window in excellent agreement with experiments. The dominant contribution arises from rotational oxygen phonons, while breathing modes contribute little. Our results establish strong EPC in cuprates, highlight the key role of rotational phonons, and provide a framework for understanding spectral anomalies in cuprates and beyond.

Despite nearly four decades of extensive research, the pairing mechanism responsible for high-temperature superconductivity ( $T_c$ ) in cuprates remains unresolved [1–4]. Cuprates are widely regarded as prototypical strongly correlated materials: superconductivity emerges upon doping a Mott or charge-transfer-insulating antiferromagnetic parent compound, and the resulting phase diagram hosts a wealth of correlation-driven phenomena. These include predominantly  $d$ -wave pairing, strange-metal transport characterized by a near-linear temperature dependence of the resistivity near optimal doping,

unusually large magnetic exchange interactions, and a variety of intertwined electronic orders [5–15].

Although this phenomenology has traditionally motivated theories emphasizing purely electronic mechanisms, a growing body of experimental evidence points to an essential role of lattice degrees of freedom in cuprates. Momentum-resolved scattering experiments have revealed pronounced phonon anomalies that track intertwined orders such as stripes and charge-density waves [16], and spectroscopic probes report broad bosonic signatures together with measurable oxygen-isotope effects [17]. Angle-resolved photoemission spectroscopy (ARPES) has provided particularly direct insight, revealing a rapid evolution of superconductivity and electron–phonon coupling (EPC) in  $\text{Bi-2212}$  ( $\text{Bi}_2\text{Sr}_2\text{CaCu}_2\text{O}_{8+\delta}$ ) [18]. More broadly, a large body of ARPES studies has established that low-energy electronic excitations near the Fermi level couple strongly to bosonic modes [19–33], giving rise to ubiquitous quasiparticle “kinks” across the cuprate family.

These kinks were long classified into two characteristic energy scales: a nodal kink near  $\sim 70$  meV [19–30] and an antinodal kink near  $\sim 40$  meV [24, 25, 28–33]. Their microscopic origin remains a subject of active debate. Both phonons [19, 22, 31] and spin fluctuations [20, 34–36] have been proposed as relevant bosonic excitations. In particular, recent ultrahigh-resolution ARPES measurements have reported kinks near  $\sim 70$  and  $\sim 40$  meV in both the nodal and antinodal directions that are largely insensitive to temperature and doping [37]. This robustness disfavors a purely magnetic origin and increasingly points to EPC as the dominant mechanism behind these photoemission features. Taken together, these observations highlight a central role for EPC in cuprates, operating alongside strong electronic correlations. From a theoretical perspective, the role of EPC in cuprates has long been controversial. Early density-functional theory (DFT) calculations suggested that EPC is too weak to account for the experimentally observed kinks [38]. However, this conclusion has been questioned [39, 40], as conventional DFT approximations—such as the local density approximation (LDA) and the Perdew–Burke–Ernzerhof (PBE) generalized gradient approximation—

\* These authors contributed equally to this work

† Corresponding author: [ar.bansil@neu.edu](mailto:ar.bansil@neu.edu)

‡ Corresponding author: [jsun@tulane.edu](mailto:jsun@tulane.edu)

§ These authors contributed equally to this work; Corresponding author: [rzhang16@tulane.edu](mailto:rzhang16@tulane.edu)

often fail to capture the electronic structure, phonon properties, and correlated magnetism of cuprates [41–45]. More recently, GW perturbation theory (GWPT) calculations have revealed a correlation-enhanced EPC, yielding EPC strengths  $\lambda$  (where  $\lambda$  is the dimensionless EPC constant) that are two to three times larger than those obtained from standard DFT [40]. These results suggest that phonon-mediated interactions alone could, in principle, explain the observed kinks. Importantly, however, both the early DFT [38] and GWPT [40] studies relied on nonmagnetic (NM) reference states and neglected magnetic effects, despite growing evidence that magnetism and spin fluctuations are intrinsic to cuprate physics [46].

These considerations demonstrate the need for an unbiased, materials-specific assessment of EPC in cuprates that treats spin, charge, orbital, and lattice degrees of freedom on equal footing. Such an approach is essential for identifying the phonon modes responsible for the ARPES kinks and for revealing whether magnetism qualitatively reshapes the electron–phonon interaction itself.

To address this challenge, we investigate EPC in hole-doped infinite-layer  $\text{CaCuO}_2$  by employing the strongly Constrained and Appropriately Normed (SCAN) density functional, explicitly incorporating magnetic effects in our calculations. We find that magnetism dramatically enhances EPC in cuprates: the total coupling strength  $\lambda$  reaches values as large as 0.5, nearly five times larger than in the nonmagnetic configuration. This strong coupling produces pronounced quasiparticle kinks and characteristic peak–dip–hump (PDH) structures in the calculated spectral function, in excellent agreement with experimental observations. Strikingly, we identify rotational phonon modes associated with oxygen vibrations as the dominant contributors to the enhanced EPC, accounting for approximately 80% of the total coupling and largely generating the high-energy dip and hump features in the photoemission lineshape. By contrast, the traditionally emphasized oxygen-breathing modes contribute only weakly. Our results provide mode-resolved microscopic insight into EPC in cuprates and reveal magnetism as a key amplifier of lattice-mediated interactions, motivating further experimental and theoretical exploration.

**Results**—As prototypical correlated materials, cuprates not only hold promise for next-generation quantum technology applications but also provide a stringent testbed for many-body theory. Our previous work has shown that the advanced SCAN functional yields more reliable electronic structures and phonon dispersions for cuprates than conventional LDA and PBE functionals [41–45]. In addition, our recent work highlights the strong transferability of the  $r^2$ SCAN/SCAN density functional for predicting EPC both accurately and efficiently across a wide range of materials—from itinerant  $s/p$ -electron systems to strongly correlated  $d$ -electron compounds [47, 48]. To assess SCAN’s performance for EPC in cuprates, we first compute the EPC of pristine  $\text{CaCuO}_2$  with both the high-energy nonmagnetic (NM) and low-energy  $G$ -

type antiferromagnetic ( $G$ -AFM) configurations. We find very weak coupling in the NM configuration ( $\lambda \approx 0.1$ ), whereas the  $G$ -AFM phase exhibits substantially stronger EPC. The weak EPC in the NM phase is consistent with earlier LDA calculations [38], while the predicted strong EPC in the  $G$ -AFM phase is consistent with a recent PBE+ $U$  study [49]. These results indicate that SCAN can deliver more reliable EPC predictions for cuprates without introducing any Hubbard- $U$  parameters. A detailed discussion of the undoped case is provided in the Supplementary Material (SM).

In the main text, we focus on the more interesting hole-doped  $G$ -AFM case. We choose a doping level of 25%, close to the experimentally relevant overdoped regime [37]. Our previous work has shown that several low-energy magnetic configurations compete closely with the  $G$ -AFM configuration in doped cuprates [43]. Since these states exhibit similar electronic structures, we take the  $G$ -AFM phase as a representative reference for assessing EPC in the doped regime [43]. The electronic structure of the doped phase is shown in Fig. S3. Upon hole doping, the metal–insulator transition is well captured in our calculations, where the lower Hubbard  $3d_{x^2-y^2}$  band crosses the Fermi level, resulting in metallic behavior.

**Strongly coupled phonons**—The calculated phonon dispersion, phonon density of states (PhDOS), and isotropic Eliashberg spectral function  $\alpha^2F(\omega)$  are shown in the left, middle, and right panels of Fig. 1(a), respectively. The color scale on the phonon dispersion indicates the mode-resolved EPC strength  $\lambda_{qv}$ . Several branches exhibiting strong coupling are found in our calculations, most prominently the high-frequency oxygen stretching and circular modes, which dominate  $\alpha^2F(\omega)$  in the 50–70 meV range. Lower-frequency modes involving Cu and Ca motions also contribute, giving rise to weaker peaks near 42 and 38 meV in  $\alpha^2F(\omega)$  [see Fig. 1(a)]. Integrating over all phonons yields a total coupling strength  $\lambda$  of  $\sim 0.5$ —approximately five times larger than that in the NM configuration—highlighting a substantial enhancement of EPC by magnetic effects. The estimated  $\omega_{\text{log}}$  is around 56.3 meV, leading to a predicted superconducting transition temperature  $T_c$  in the range of 8–17 K, depending on the choice of Coulomb pseudopotential  $\mu^*$  between 0.10 and 0.04. Note that the optimal  $T_c$  observed at the  $\text{CaCuO}_2/\text{SrTiO}_3$  interface is around 40 K [50]. These results show that the AFM state hosts a rich variety of phonon modes which can play distinct roles in cuprate physics, highlighting clear qualitative differences between the NM and AFM phases.

Representative phonon eigenmodes that contribute strongly to the EPC are shown in Fig. 1 (e)–(h). Panels (e)–(g) sample points on the O-derived branches between 50–70 meV [see labeled points in the left panel of Fig. 1(a)]. At high-symmetry points, the  $\Gamma_1$  and  $X_1$  modes correspond to an in-plane full-breathing and a quadrupolar oxygen vibration, respectively. More interestingly, away from high-symmetry lines, the eigenvectors are generally rotational within the  $ab$ -plane. For

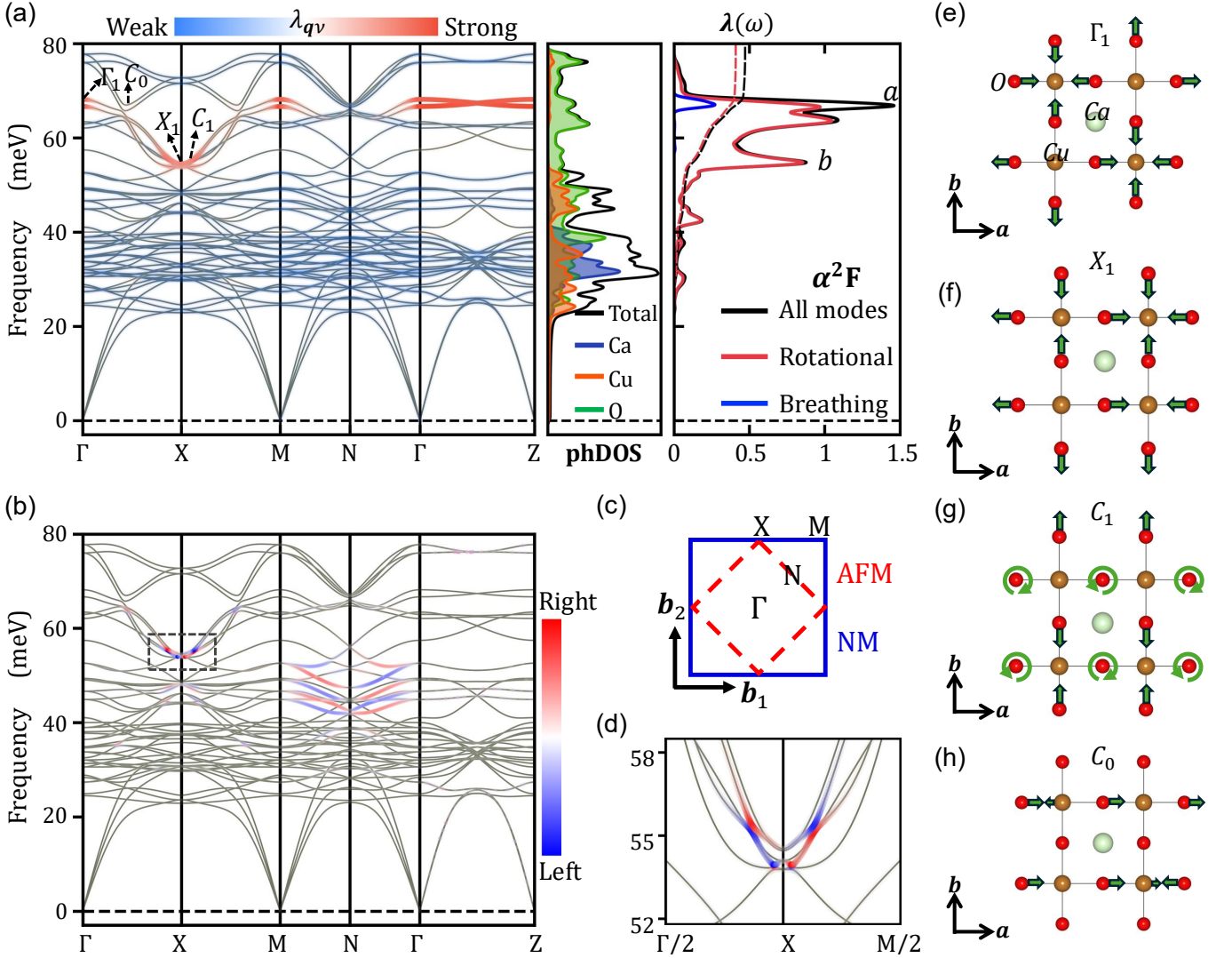


FIG. 1. **Calculated phonon dispersion and EPC of G-AFM phase of CaCuO<sub>2</sub> with 25% hole doping.** (a) Left panel: calculated folded phonon dispersion along high-symmetry lines in the first BZ; marker color-intensity indicates the value of the EPC strength,  $\lambda_{q\nu}$ , for the doped phase; Middle panel: site-projected phonon density of states (PhDOS). Right panel: calculated Eliashberg spectral functions,  $\alpha^2 F(\omega)$  (solid red lines), and the cumulative EPC strength,  $\lambda$  (dashed blue lines). A  $k$ -mesh of  $60 \times 60 \times 60$  and a  $q$ -mesh of  $30 \times 30 \times 30$  were used for full BZ sampling. (b) Phonon dispersion color-coded by the  $z$ -component of the circular polarization for vibrations of four representative oxygen sites in the same sense. Red, blue, and gray denote right-handed ( $s_{\mathbf{q},\sigma}^\alpha > 0$ ), left-handed ( $s_{\mathbf{q},\sigma}^\alpha < 0$ ), and non-polarized ( $s_{\mathbf{q},\sigma}^\alpha = 0$ ) phonon modes. (c) Schematic of the NM and AFM BZs in the  $k_z = 0$  plane, with high-symmetry points marked. (d) Closeup of the area marked by the black-dashed rectangle in (b) to highlight the rotational phonon modes. (e)-(h) Side view of selected phonon modes marked at (b), with green arrows representing the direction of atomic vibrations. Brown, light green, and red balls represent Cu, Ca, and O atoms, respectively.

instance, the mode in panel (g) combines rotational phonons along  $z$  with a half-breathing mode along  $y$ . Interestingly, we also observed a softening characteristic associated with the  $C_0$  branch at  $\mathbf{q} = (0.22, 0, 0)$  around  $\sim 65$  meV, close to the experimentally reported charge-density-wave (CDW) wave vector  $\mathbf{q}_{\text{CDW}} = (0.25, 0, 0)$ . The  $C_0$  mode has predominantly half-breathing character involving O and Cu motions, as illustrated in Fig. 1(h). We discuss the connection to the experimental CDW phenomenology in the SM.

To quantify the chirality of the phonon modes, we evaluate the phonon circular polarization (angular momentum) following the formalism introduced in earlier work [51, 52]. Specifically, we compute

$$s_{\mathbf{q},\sigma}^\alpha = \sum_{i=1}^N \mathbf{e}_{i,\mathbf{q},\sigma}^\dagger S^\alpha \mathbf{e}_{i,\mathbf{q},\sigma}, \quad (1)$$

where  $\mathbf{e}_{i,\mathbf{q},\sigma}$  is the phonon eigenvector for wave vector  $\mathbf{q}$ , branch index  $\sigma$ , and atom index  $i$ , and  $S^\alpha$  ( $\alpha = x, y, z$ )

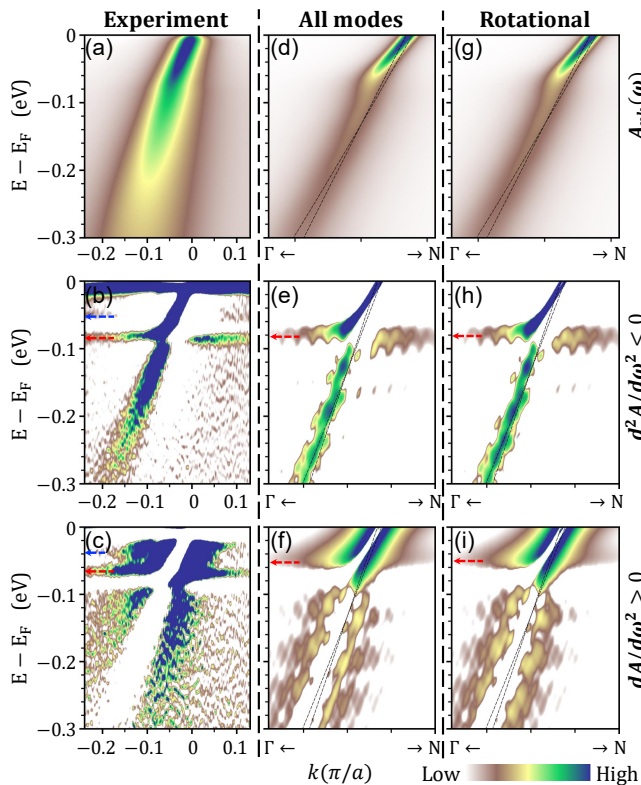


FIG. 2. **Comparison of the experimental and calculated spectral functions** (a)-(c) Measured ARPES spectra at  $T = 20K$  for Bi2201 with a similar hole doping level of approximately 20%, extracted from Ref. [37]. Red arrows indicate high-energy humps and dips, while blue arrows indicate low-energy ones. (d) Calculated spectral function along the  $\Gamma$ - $N$  direction. (e) shows the second derivative of the spectral function with respect to energy, showing the absolute magnitude of the negative values, while (c) presents the corresponding positive components. Red arrows indicate high-energy humps and peaks. (g)-(i) same as (d)-(f), but only considering the rotational phonon contributions. Note that peaks in the second derivative correspond to dips in the phonon spectrum, and vice versa.

are the spin-1 matrices in the Cartesian basis. The sign of  $s_{\mathbf{q},\sigma}^{\alpha}$  encodes the handedness of the mode:  $s_{\mathbf{q},\sigma}^{\alpha} < 0$  ( $> 0$ ) corresponds to a right-handed (left-handed) circularly polarized phonon with respect to axis  $\alpha$ .

Figure 1(b) displays the  $z$ -component of the circular polarization for oxygen-dominated phonon modes. We identify three sets of rotational branches along the high-symmetry lines: two oxygen optical modes—one near  $\sim 55$  meV along  $\Gamma$ - $X$ - $M$  and another near  $\sim 45$  meV along  $M$ - $N$ - $\Gamma$  [see Fig. 1(c)], and a low-energy branch associated with acoustic modes involving Ca motions (similar to the doped NM mode in Fig.S4). The most important branches are non-chiral: although individual oxygen atoms rotate clockwise (CW) or counterclockwise (CCW), equal numbers rotate in opposite directions, yielding zero net chirality, as in Fig. 1(g). In panels (b) and (d), we plot a collective chirality defined

as the sum of the circular-polarization projections from four representative oxygen sites ( $O_1, O_3, O_6$ , and  $O_8$ ) out of the eight oxygen atoms in the AFM unit cell. The site-resolved chirality for each oxygen atom is shown in Fig. S5, making it clear that these four oxygens rotate in the same sense, whereas the other four all rotate in the opposite sense, leading to vanishing net polarization.

Importantly, these strongly coupled rotational modes emerge only in the doped AFM configuration. The reason for that is that in the NM phase, many optical branches are degenerate with orthonormal eigenvectors indicated as linearly polarized. In the AFM state, time-reversal symmetry is broken, which lifts these degeneracies and selects circularly polarized eigenstates, thereby making the chirality directly manifest in the calculated phonon modes. In addition, both the AFM and NM phases host rotational character in the two degenerate transverse acoustic modes along  $\Gamma$ - $Z$ , arising from the vibrations of Ca atoms (see Fig. S4 and S5). However, these acoustic rotational branches couple only weakly to the electrons.

Comparing Fig. 1(a) and (b) shows that the rotational phonons are also the phonon modes most strongly coupled to electrons. The mode-decomposed  $\alpha^2 F(\omega)$  in the right panel of Fig. 1(a) reveals that rotational oxygen vibrations contribute  $\sim 80\%$  of the total EPC, corresponding to  $\lambda_{\text{rotational}} \approx 0.4$ , and dominate peaks  $a$  and  $b$  in the  $\alpha^2 F(\omega)$ . Beyond these, several non-rotational modes show noticeable EPC, such as the full- and half-breathing modes from oxygen [see the blue lines in the right panel of Fig. 1(a)]. However, the breathing-mode contribution is tiny:  $\lambda_{\text{breathing}} \approx 0.01$ , corresponding to only  $\sim 2\%$  of the total EPC. This challenges the conventional view that breathing modes play a dominant role in cuprates.

**Low-energy kinks**—Figure 2(d)-(f) shows the calculated spectral function along the nodal direction of hole-doped  $\text{CaCuO}_2$ . We find pronounced band renormalization and quasiparticle broadening in the 40–80 meV window [see Fig. 2(d)], in excellent agreement with ARPES observations of nodal dispersion kinks in cuprates [see Fig. 2(a)] [37]. A second-derivative analysis of the spectral function highlights a high-energy hump near  $\sim 80$  meV [Fig. 2(e)] and a high-energy dip feature near  $\sim 50$  meV [Fig. 2(f)], close to the experimental values of  $\sim 86$  and  $\sim 67$  meV, respectively [see Figs. 2 (b) and 2(c) respectively.] [37]. These results demonstrate that our calculations capture the well-known “peak-dip-hump” structure in cuprates.

The mode-decomposed spectral functions in Fig. 2(g)-(i) show that rotational oxygen phonons dominate the key spectral features in our calculations, indicating that the experimentally observed  $\sim 40$  meV kink is most naturally associated with rotational branches such as  $C_1$ , rather than the oxygen bond-bending modes proposed previously [31]. The hump feature is likewise governed primarily by rotational modes, with breathing-like modes providing only a minor contribution [see Fig. 2(e) and (h)]. Overall, these results suggest that the ubiquitous  $\sim 70$  meV kink is strongly influenced by the rotational

oxygen modes identified above, rather than being dominated by the conventionally assumed zone-centre breathing mode alone.

Notice that there are still some differences between our predictions and experiments. For example, our calculations show a single hump and a single dip on each side [see Fig. 2(e) and Fig. 2(f)], whereas ARPES on Bi-based cuprates reports double-hump and double-dip features [see Fig. 2(b) and Fig. 2(c)]. These discrepancies likely reflect (i) the different systems studied—our theory treats the infinite-layer  $\text{CaCuO}_2$  while the measurements are on Bi-based cuprates—and (ii) multiple competing orders in doped cuprates [43, 53], like stripe and charge-density-wave (CDW) phases, that are not included in our single-phase calculation. We further note that the second hump and dip features are relatively weak in the experiment, and were not observed in earlier, lower-resolution ARPES studies.

*Discussion*—Our results show that the interaction between electrons and lattice vibrations plays a central role in cuprate superconductors. In particular, our calculations reproduce well-known experimental features such as the characteristic kinks in the electronic spectra and the peak–dip–hump line shape. More importantly, they reveal that the dominant coupling does not arise from the commonly assumed oxygen-breathing modes but is instead driven by *rotational oxygen phonons*. This finding has broader implications in light of the thermal Hall effect observed in cuprates, which appears in the pseudogap regime and vanishes when the pseudogap closes, and has been proposed to originate from phonons carrying angular momentum [54]. Our results provide microscopic insight into the properties of these phonons: the rotational modes that couple most strongly to the electrons emerge only in the doped magnetic phase and are absent in the nonmagnetic phase (see SM Fig. S4(e)). Identifying these rotational phonons as the origin of the thermal Hall effect [55, 56] would therefore lend strong support to the idea that the pseudogap corresponds to a form of short-range antiferromagnetic order [57].

It has long been suggested that strong EPC, when combined with strong electronic correlations and/or antiferromagnetic fluctuations, can promote high-temperature superconductivity with  $d$ -wave pairing symmetry [58, 59]. Although there has recently been debate about whether isotropic EPC alone can lead to  $d$ -wave pairing [60, 61], an important result of Ref. [58] is that the effect is strongest for highly anisotropic EPC, in particular for coupling dominated by forward scattering, as may be expected near a peak in the electronic density of states. In this context, it is noteworthy that recent DFT+ $U$  calculations have reported strong EPC in the parent compound  $\text{La}_2\text{CuO}_4$  when local magnetism is included [49],

although not associated with rotational phonons (see also SM Section S-III). In addition, a toy-model study suggests that explaining the low-energy kinks observed in cuprates likely requires the intertwined effects of both EPC and electronic correlations [62].

Notably, it was recently shown that bond Su–Schrieffer–Heeger (SSH) phonons—that is, phonons that modulate the electronic hopping amplitude  $t$ —can cooperate with strong correlations to produce  $d$ -wave superconductivity in a phase characterized by strong antiferromagnetic fluctuations [57, 59]. Our results add a new element to this emerging picture: in cuprates, as well as nickelates we studied in Ref. [48, 63], strong (and fluctuating) antiferromagnetic order itself generates enhanced EPC. Remarkably, this occurs even though different phonons dominate the coupling in the two materials. In nickelates, the dominant EPC arises from low-energy La/Ni modes that couple strongly to a flat electronic band of  $d_{z^2}$  character [48, 63], rather than from the rotational oxygen phonons that dominate in cuprates. This points to magnetism-enhanced EPC as a unifying mechanism across different families of unconventional superconductors, despite substantial differences in their lattice dynamics and electronic structure. Although we have focused on the central role of rotational phonons, our calculations also shed light on the charge-density-wave instability, as discussed in Supplementary Section S-VII.

*Conclusion*—We have investigated electron–phonon coupling (EPC) in the infinite-layer cuprate  $\text{CaCuO}_2$  using advanced density-functional-theory methods that explicitly account for magnetism. We find that magnetism dramatically enhances EPC in cuprates: upon doping, the coupling strength  $\lambda$  reaches values of order 0.5, nearly five times larger than in the nonmagnetic phase. The resulting kink magnitude and the characteristic peak–dip–hump line shape obtained in the presence of copper magnetic moments are in close quantitative agreement with experiment. Crucially, we show that this enhanced coupling is not dominated by conventional oxygen-breathing modes but instead arises primarily from rotational oxygen phonons, revising the standard picture of EPC in cuprates. These magnetism-enabled rotational modes naturally connect electronic structure anomalies to lattice dynamics and provide a microscopic framework for understanding experimental signatures associated with the pseudogap and charge-density-wave tendencies. Taken together, our results identify *magnetism-induced electron–phonon coupling*, mediated by rotational oxygen phonons, as a key and previously unrecognized ingredient linking the pseudogap, anomalous thermal transport, and superconductivity in cuprates, and suggest a unifying mechanism that may extend to other strongly correlated materials.

---

[1] Damascelli, A., Hussain, Z. & Shen, Z.-X. Angle-resolved photoemission studies of the cuprate superconductors.

*Rev. Mod. Phys.* **75**, 473–541 (2003).

- [2] Sobota, J. A., He, Y. & Shen, Z.-X. Angle-resolved photoemission studies of quantum materials. *Rev. Mod. Phys.* **93**, 025006 (2021).
- [3] Varma, C. M. Colloquium: Linear in temperature resistivity and associated mysteries including high temperature superconductivity. *Rev. Mod. Phys.* **92**, 031001 (2020).
- [4] Norman, M. R. The challenge of unconventional superconductivity. *Science* **332**, 196–200 (2011).
- [5] Kivelson, S. A. *et al.* How to detect fluctuating stripes in the high-temperature superconductors. *Rev. Mod. Phys.* **75**, 1201–1241 (2003).
- [6] Fradkin, E., Kivelson, S. A. & Tranquada, J. M. Colloquium: Theory of intertwined orders in high temperature superconductors. *Rev. Mod. Phys.* **87**, 457–482 (2015).
- [7] Dagotto, E. Complexity in Strongly Correlated Electronic Systems. *Science* **309**, 257–262 (2005).
- [8] Emery, V. J., Kivelson, S. A. & Tranquada, J. M. Stripe phases in high-temperature superconductors. *Proc. Natl. Acad. Sci.* **96**, 8814–8817 (1999).
- [9] Hanaguri, T. *et al.* A ‘checkerboard’ electronic crystal state in lightly hole-doped  $\text{Ca}_{2-x}\text{Na}_x\text{CuO}_2\text{Cl}_2$ . *Nature* **430**, 1001–1005 (2004).
- [10] Kohsaka, Y. *et al.* An Intrinsic Bond-Centered Electronic Glass with Unidirectional Domains in Underdoped Cuprates. *Science* **315**, 1380–1385 (2007).
- [11] Pan, S. H. *et al.* Microscopic electronic inhomogeneity in the high- $T_c$  superconductor  $\text{Bi}_2\text{Sr}_2\text{CaCu}_2\text{O}_{8+x}$ . *Nature* **413**, 282–285 (2001).
- [12] Jiang, H.-C. & Kivelson, S. A. Stripe order enhanced superconductivity in the Hubbard model. *Proc. Natl. Acad. Sci.* **119**, 32–34 (2022).
- [13] Tranquada, J. M., Sternlieb, B. J., Axe, J. D., Nakamura, Y. & Uchida, S. Evidence for stripe correlations of spins and holes in copper oxide superconductors. *Nature* **375**, 561–563 (1995).
- [14] Zheng, B.-X. *et al.* Stripe order in the underdoped region of the two-dimensional Hubbard model. *Science* **358**, 1155–1160 (2017).
- [15] Huang, E. W. *et al.* Numerical evidence of fluctuating stripes in the normal state of high- $T_c$  cuprate superconductors. *Science* **358**, 1161–1164 (2017).
- [16] Li, J. *et al.* Multiorbital charge-density wave excitations and concomitant phonon anomalies in  $\text{Bi}_2\text{Sr}_2\text{LaCuO}_{6+\delta}$ . *Proceedings of the National Academy of Sciences* **117**, 16219–16225 (2020).
- [17] Lee, J. *et al.* Interplay of electron–lattice interactions and superconductivity in  $\text{Bi}_2\text{Sr}_2\text{CaCu}_2\text{O}_{8+\delta}$ . *Nature* **442**, 546–550 (2006).
- [18] He, Y. *et al.* Rapid change of superconductivity and electron-phonon coupling through critical doping in  $\text{Bi}_2\text{Sr}_2\text{CaCu}_2\text{O}_{8+\delta}$ . *Science* **362**, 62–65 (2018).
- [19] Bogdanov, P. V. *et al.* Evidence for an energy scale for quasiparticle dispersion in  $\text{Bi}_2\text{Sr}_2\text{CaCu}_2\text{O}_8$ . *Phys. Rev. Lett.* **85**, 2581–2584 (2000).
- [20] Johnson, P. D. *et al.* Doping and temperature dependence of the mass enhancement observed in the cuprate  $\text{Bi}_2\text{Sr}_2\text{CaCu}_2\text{O}_{8+\delta}$ . *Phys. Rev. Lett.* **87**, 177007 (2001).
- [21] Kaminski, A. *et al.* Renormalization of spectral line shape and dispersion below  $T_c$  in  $\text{Bi}_2\text{Sr}_2\text{CaCu}_2\text{O}_{8+\delta}$ . *Phys. Rev. Lett.* **86**, 1070–1073 (2001).
- [22] Lanzara, A. *et al.* Evidence for ubiquitous strong electron–phonon coupling in high-temperature superconductors. *Nature* **412**, 510–514 (2001).
- [23] Zhou, X. J. *et al.* Universal nodal fermi velocity. *Nature* **423**, 398 (2003).
- [24] Gromko, A. D. *et al.* Mass-renormalized electronic excitations at  $(\pi, 0)$  in the superconducting state of  $\text{Bi}_2\text{Sr}_2\text{CaCu}_2\text{O}_{8+\delta}$ . *Phys. Rev. B* **68**, 174520 (2003).
- [25] Sato, T. *et al.* Observation of band renormalization effects in hole-doped high- $T_c$  superconductors. *Phys. Rev. Lett.* **91**, 157003 (2003).
- [26] Kordyuk, A. A. *et al.* Constituents of the quasiparticle spectrum along the nodal direction of high- $T_c$  cuprates. *Phys. Rev. Lett.* **97**, 017002 (2006).
- [27] Zhang, W. *et al.* Identification of a new form of electron coupling in the  $\text{Bi}_2\text{Sr}_2\text{CaCu}_2\text{O}_8$  superconductor by laser-based angle-resolved photoemission spectroscopy. *Phys. Rev. Lett.* **100**, 107002 (2008).
- [28] He, J. *et al.* Coexistence of two sharp-mode couplings and their unusual momentum dependence in the superconducting state of  $\text{Bi}_2\text{Sr}_2\text{CaCu}_2\text{O}_{8+\delta}$  revealed by laser-based angle-resolved photoemission. *Phys. Rev. Lett.* **111**, 107005 (2013).
- [29] Kondo, T. *et al.* Anomalous doping variation of the nodal low-energy feature of superconducting  $(\text{Bi,Pb})_2(\text{Sr,L a})_2\text{CuO}_{6+\delta}$  crystals revealed by laser-based angle-resolved photoemission spectroscopy. *Phys. Rev. Lett.* **110**, 217006 (2013).
- [30] Anzai, H. *et al.* A new landscape of multiple dispersion kinks in a high- $T_c$  cuprate superconductor. *Scientific Reports* **7**, 4830 (2017).
- [31] Cuk, T. *et al.* Coupling of the  $B_{1g}$  phonon to the antinodal electronic states of  $\text{Bi}_2\text{Sr}_2\text{Ca}_{0.92}\text{Y}_{0.08}\text{Cu}_2\text{O}_{8+\delta}$ . *Phys. Rev. Lett.* **93**, 117003 (2004).
- [32] Kim, T. K. *et al.* Doping dependence of the mass enhancement in  $(\text{Pb,Bi})_2\text{Sr}_2\text{CaCu}_2\text{O}_8$  at the antinodal point in the superconducting and normal states. *Phys. Rev. Lett.* **91**, 167002 (2003).
- [33] Cuk, T. *et al.* Coupling of the  $B_{1g}$  phonon to the antinodal electronic states of  $\text{Bi}_2\text{Sr}_2\text{Ca}_{0.92}\text{Y}_{0.08}\text{Cu}_2\text{O}_{8+\delta}$ . *Phys. Rev. Lett.* **93**, 117003 (2004).
- [34] Byczuk, K. *et al.* Kinks in the dispersion of strongly correlated electrons. *Nature Physics* **3**, 168–171 (2007).
- [35] Dahm, T. *et al.* Strength of the spin-fluctuation-mediated pairing interaction in a high-temperature superconductor. *Nature Physics* **5**, 217–221 (2009).
- [36] Eschrig, M. & Norman, M. R. Dispersion anomalies in bilayer cuprates and the odd symmetry of the magnetic resonance. *Phys. Rev. Lett.* **89**, 277005 (2002).
- [37] Yan, H. *et al.* Ubiquitous coexisting electron-mode couplings in high-temperature cuprate superconductors. *Proceedings of the National Academy of Sciences* **120**, e2219491120 (2023).
- [38] Giustino, F., Cohen, M. L. & Louie, S. G. Small phonon contribution to the photoemission kink in the copper oxide superconductors. *Nature* **452**, 975–978 (2008).
- [39] Reznik, D., Sangiovanni, G., Gunnarsson, O. & Devereaux, T. P. Photoemission kinks and phonons in cuprates. *Nature* **455**, E6–E7 (2008).
- [40] Li, Z., Wu, M., Chan, Y.-H. & Louie, S. G. Unmasking the origin of kinks in the photoemission spectra of cuprate superconductors. *Phys. Rev. Lett.* **126**, 146401 (2021).
- [41] Furness, J. W. *et al.* An accurate first-principles treatment of doping-dependent electronic structure of high-temperature cuprate superconductors. *Communications Physics* **1**, 11 (2018).

- [42] Lane, C. *et al.* Antiferromagnetic ground state of  $\text{La}_2\text{CuO}_4$ : A parameter-free *ab-initio* description. *Physical Review B* **98**, 125140 (2018).
- [43] Zhang, Y. *et al.* Competing stripe and magnetic phases in the cuprates from first principles. *Proceedings of the National Academy of Sciences* **117**, 68–72 (2020).
- [44] Ning, J. *et al.* Critical role of magnetic moments in the lattice dynamics of  $\text{YBa}_2\text{Cu}_3\text{O}_6$ . *Phys. Rev. B* **107**, 045126 (2023).
- [45] Ning, J. *et al.* Comparing first-principles density functionals plus corrections for the lattice dynamics of  $\text{YBa}_2\text{Cu}_3\text{O}_6$ . *The Journal of Chemical Physics* **160**, 064106 (2024).
- [46] Tranquada, J. M. *et al.* Quantum magnetic excitations from stripes in copper oxide superconductors. *Nature* **429**, 534–538 (2004).
- [47] Wang, Y. *et al.* Accurate electron-phonon interactions from advanced density functional theory. *PRX Energy* **5**, 013002 (2026).
- [48] Zhang, R. *et al.* Magnetism-enhanced strong electron-phonon coupling in infinite-layer nickelates. *Phys. Rev. B* **112**, L241115 (2025).
- [49] Chang, B. K. *et al.* First-principles electron-phonon interactions and polarons in the parent cuprate  $\text{La}_2\text{CuO}_4$ . *Phys. Rev. Res.* **7**, L012073 (2025).
- [50] Di Castro, D. *et al.* High- $T_c$  superconductivity at the interface between the  $\text{CaCuO}_2$  and  $\text{SrTiO}_3$  insulating oxides. *Phys. Rev. Lett.* **115**, 147001 (2015).
- [51] Zhang, L. & Niu, Q. Chiral phonons at high-symmetry points in monolayer hexagonal lattices. *Phys. Rev. Lett.* **115**, 115502 (2015).
- [52] Pols, M., Brocks, G., Calero, S. & Tao, S. Chiral phonons in 2D halide perovskites. *Nano Letters* **25**, 10003–10009 (2025).
- [53] Markiewicz, R. S. & Bansil, A. Theory of cuprate pseudogap as antiferromagnetic order with charged domain walls. *Phys. Rev. B* **109**, 045116 (2024).
- [54] Grissonnanche, G. *et al.* Chiral phonons in the pseudogap phase of cuprates. *Nature Physics* **16**, 1108–1111 (2020).
- [55] Lizaire, M. *et al.* Transport signatures of the pseudogap critical point in the cuprate superconductor  $\text{Bi}_2\text{Sr}_{2-x}\text{La}_x\text{CuO}_{6+\delta}$ . *Phys. Rev. B* **104**, 014515 (2021).
- [56] Sapkota, A. *et al.* Reinvestigation of crystal symmetry and fluctuations in  $\text{La}_2\text{CuO}_4$ . *Phys. Rev. B* **104**, 014304 (2021).
- [57] Cai, X., Li, Z.-X. & Yao, H. Antiferromagnetism induced by bond su-schrieffer-heeger electron-phonon coupling: A quantum monte carlo study. *Phys. Rev. Lett.* **127**, 247203 (2021).
- [58] Kulić, M. L. Interplay of electron-phonon interaction and strong correlations: the possible way to high-temperature superconductivity. *Physics Reports* **338**, 1–264 (2000).
- [59] Wang, H.-X., Jiang, Y.-F. & Yao, H. Robust d-wave superconductivity from the su-schrieffer-heeger-hubbard model: possible route to high-temperature superconductivity. *Science Bulletin* **70**, 2260–2265 (2025).
- [60] Schrodi, F., Oppeneer, P. M. & Aperis, A. Unconventional superconductivity mediated solely by isotropic electron-phonon interaction. *Phys. Rev. B* **104**, L140506 (2021).
- [61] Dee, P. M., Cohen-Stead, B., Johnston, S. & Hirschfeld, P. J. Charge correlations suppress unconventional pairing in the holstein model. *Phys. Rev. B* **107**, 104503 (2023).
- [62] Huang, E. W. *et al.* Extracting correlation effects from momentum-resolved electron energy loss spectroscopy: Synergistic origin of the dispersion kink in  $\text{Bi}_{2.1}\text{Sr}_{1.9}\text{CaCu}_2\text{O}_{8+x}$ . *Phys. Rev. B* **103**, 035121 (2021).
- [63] Zhang, R. *et al.* Emergence of competing stripe phases in undoped infinite-layer nickelates. *Phys. Rev. Lett.* **133**, 066401 (2024).

*Acknowledgements*—We thank Dr. Hongtao Yan and Prof. X.J. Zhou for helpful discussions on the cuprates. Y.W., R.Z., J.P.P. and J.S. acknowledge the support of the U.S. National Science Foundation under Grant No. CHE-2533416. A.R. acknowledges the U.S. National Science Foundation under Grant No. CHE-2533416 for the meta-GGA work. For the work on superconductors with electron-phonon interaction, A.R. acknowledges the U.S. Department of Energy, Office of Science, Office of Basic Energy Sciences, under Award Number DE-SC0026293. R.Z. and J.S. also acknowledges the support of the American Chemical Society Petroleum Research Fund, grant number: PRF#69244-ND10. The work at Tulane University was also supported by the Advanced Cyberinfrastructure Coordination Ecosystem funded by the National Science Foundation, and the National Energy Research Scientific Computing Center (NERSC) using NERSC Awards No. BES-ERCAP0020494 and No. BESER-CAP0028709. The work at Northeastern University was supported by the National Science Foundation through the Expand-QISE award NSF-OMA-2329067 and benefited from the resources of Northeastern University’s Advanced Scientific Computation Center, the Discovery Cluster, and the Massachusetts Technology Collaborative award MTC-22032. The work at Los Alamos National Laboratory was carried out under the auspices of the U.S. Department of Energy (DOE) National Nuclear Security Administration under Contract No. 89233218CNA000001. It was supported by the LANL LDRD Program, the Quantum Science Center, a U.S. DOE Office of Science National Quantum Information Science Research Center, and in part by the Center for Integrated Nanotechnologies, a DOE BES user facility, in partnership with the LANL Institutional Computing Program for computational resources. Additional computations were performed at the NERSC, a U.S. Department of Energy Office of Science User Facility located at Lawrence Berkeley National Laboratory, operated under Contract No. DE-AC02-05CH11231 using NERSC Award No. ERCAP0020494. B. B. acknowledges support from the COST Action CA16218.

*Author contributions*—R.Z., J.S., and A.B. designed the study. Y.W., M.E., and R.Z. performed first principles computations and analyzed the data with help from C.L., H.M., B.B., R.S.M., J.Z., G. K., A.B., and J.S. A.B. and J.S. provided computational infrastructure. R.Z., Y.W., M.E., H.M., C.L., B.B., R.S.M., A.B., G.K., and J.S. wrote the manuscript with input from all the authors. All authors contributed to editing the manuscript.

*Additional information*—The authors declare no competing financial interests.